Solvated Ion Evaporation from Charged Water Nanodroplets

Vasiliy Znamenskiy,† Ioan Marginean, and Akos Vertes*

Department of Chemistry, George Washington University, Washington, D.C. 20052

Received: March 4, 2003; In Final Form: June 18, 2003

The behavior of electrified droplets in an atmospheric environment and the mechanism of ion formation in electrospray ionization are the subject of continuing debate. Experimental evidence to decide between the various models of ion formation (e.g., ion evaporation, Coulomb explosion, and charge residue model) is not readily available and is especially scarce for nanometer-sized droplets. Even the morphology, the structure, and the dynamics of aqueous nanodroplets containing ionic solutes are poorly understood. Classical molecular dynamics simulations were used to explore the effect of ions on the shape and structure of these droplets. We also followed the gas-phase formation of hydronium and glycine homologue ions from the disintegrating nanodroplets. Droplets up to 6.5 nm in diameter were studied using potentials for the peptides and water that accounted for their internal degrees of freedom. Validity testing of the model indicated good agreement between the calculated radial distribution functions for water and corresponding neutron diffraction data. The self-diffusion coefficients and the enthalpy of evaporation derived from the model also gave good agreement with the experimental values. Our results showed that the ions were distributed in concentric layers within the droplet. This is a departure from the expectation that ions inside the droplet follow a monotonic radial distribution close to the surface because of the Coulomb repulsion and/or hydrophobic forces. Due to the presence of ions in the droplet, both overall shape deformations and enhanced surface fluctuations were observed. Charge reduction at the Rayleigh limit proceeded through the formation of transient surface protrusions. For droplets containing ions, amplitude protrusions higher than in the case of pure water droplets developed. These protrusions served as the intermediate stage preceding ion ejection. The evaporated ions detached from the droplet with a solvation shell of approximately 10 water molecules per ion. Our data were coherent with the solvated ion evaporation model for droplets close to the Rayleigh limit. To the best of our knowledge, these are the first molecular dynamics calculations on realistic charged nanodroplets to give insight into their structure and fission dynamics.

Electrified droplets play a significant role in processes in the Earth's atmosphere. Negligibly charged droplets in clouds are thought to contribute to lightning formation, whereas nanodroplets charged close to the Rayleigh limit might explain excess absorption of solar radiation.[1] Charged methane droplets in Titan's troposphere are thought to influence the climate on this fascinating moon of Saturn.[2] Radioactive radiation enhances the charging of environmental aerosols. Scavenging efficiency of droplets increases by added charge, thereby facilitating fallout.[3]

Over a century ago, Lord Rayleigh was intrigued by the behavior of charged water droplets and ice crystallites in clouds. To unravel the mystery, he devoted significant efforts to describe capillary waves on liquid jets and to understand the behavior of electrified water drops.[4−6] Throughout the twentieth century, this line of inquiry continued to attract the attention of prominent scientists, such as G. Taylor, who, among other findings, determined that electrified liquid interfaces under certain conditions assume a well-defined conical geometry.[7]

More recently, additional impetus was provided to studying electrostatic sprays by the discovery of electrospray ionization (ESI) as a reliable source of macromolecular ions[8,9] with excellent ion yield.[10] The main motivation for these studies stemmed from the need to analyze biomolecules with high accuracy and throughput. On the basis of ESI, proteins, nucleic acids, carbohydrates, and synthetic polymers have been mass analyzed with unprecedented accuracy. Using ion mobility spectroscopy, gas phase observations of protein ion conformation and folding patterns have also been made possible.[11−13]

ESI is a remarkably complex process with several distinct spatial regions of spray formation and numerous dramatically different regimes of operation. The nineties was a decade of heated debate over the mechanism of ESI. According to several participants in these discussions, by the year 2000 a consensus was beginning to emerge.[14,15] Capillary waves are presumed to be at the core of the liquid dispersion phenomena. Current oscillations are commonly observed in electrosprays,[16] and droplet breakup is considered to be initiated by surface instabilities. Highly asymmetric division of electrified droplets in the 10−100 μm size range has been observed by flash shadowgraphy.[17]

One of the prominent descriptions of ion formation in electrospray ionization is based on continued division of supercharged droplets until a single ion remains in the residue (charge residue model).[18] In the competing model, the ions are directly ejected from the supercharged droplet (ion evaporation model).[19] According to recent analysis, both of these models are feasible, although under different conditions. The ion evaporation model typically prevails for relatively small (m/z < 3300) solute ions,[20,21] whereas the charge residue model

* To whom correspondence should be addressed. E-mail: vertes@gwu.edu.
† Current address: Department of Chemistry, Brooklyn College of CUNY.

10.1021/jp034561z CCC: $25.00
Published on Web 09/03/2003

seems to be valid for larger multiply charged species.[22] Experimental evidence to decide between the ion evaporation model and the charge residue model is not readily available and is especially scarce for nanometer sized droplets.

Along with charge, viscosity of the liquid also affects the droplet partition.[23] The division of a viscous droplet into a few parts of comparable size is similar to the phenomenon described by the charge residue model, whereas the ejection of a large number of small daughter droplets may be related to the ion evaporation model. This analogy suggests that these models, at least on the nanoscale, describe the two extremes of the same general process.

Fission occurs because of the instability of capillary oscillations on the surface. At the Rayleigh limit, any perturbation of the surface induces unstable deformations that may result in droplet breakup. For nanodroplets, thermal surface fluctuations can be sufficient to create these perturbations.

The structure of aqueous droplets carrying ionic charge is believed to be governed by Coulomb repulsion between the ions, resulting in the highest charge density at the surface with monotonic descent toward the droplet center. This is further accentuated for hydrophobic ionic species that are also expelled from the interior of the droplet by hydrophobic forces. For example, a recent model[24] postulates that hydrophilic species reside closer to the center, whereas the hydrophobic species are located on the surface.

Classical molecular dynamics simulations promise a convenient way of describing the morphology, structure, and disintegration of nanodroplets in various charge states. Using molecular modeling, we followed the gas-phase formation of hydronium and glycine homologue ions from water nanodroplets. Molecular dynamics calculations were conducted on numerous realistic nanodroplets to directly observe the prevailing charge reduction mechanism.

On the basis of our experience with modeling matrix-assisted laser desorption ionization at the molecular level,[25,26] simulations were performed using version 24b2 of the CHARMM molecular modeling program.[27] To simulate different evolution periods and droplet formation conditions, a varying number of hydronium and glycine homologue ions were placed inside water droplets of various sizes, keeping the overall charge at the Rayleigh limit at the same time.

Methods

Molecular Dynamics Simulations. As in other MD simulations of droplets and clusters,[28] no boundary conditions were necessary because the droplet was placed in a vacuum environment. However, a spherical restraining potential was used for each droplet in the initialization stage. Energy minimization and MD simulation with damped dynamics and heating were performed to bring the atomic velocities to quasi-equilibrium. The dynamics integration method (Leapfrog Verlet) was based on the Verlet scheme, which provided enhanced accuracy. To reach a total time of up to 300 ps, a typical simulation employed ~300 000 steps and the coordinates were saved every 100 steps for further analysis. Calculations were performed on a Sun Ultra Enterprise 4000 system and on an SGI Origin 2000 computer. The results were analyzed using the gOpenMol visualization package on SGI and PC workstations. Numerous simulations were performed on droplets ranging from 1 to 7.5 nm in size.

Force Fields. Because CHARMM does not contain a model for the hydronium ion, we defined one on the basis of the geometry and energy parameters evaluated by ab initio calculations. These calculations were performed at the 6-31G* level using PC Spartan version 1.3 (Wavefunction, Irvine, CA). The CHARMM22 all-atom potential function was used for peptides. The glycine and glycine homologues were represented in three different states: protonated, neutral, and zwitterionic. The CHARMM force-field database provided the potential parameters for the zwitterionic form of the glycine and glycine homologues; however, it did not contain the potential constants for the carboxyl group of the protonated forms. Analogies within the CHARMM force-field database were used to estimate the potential parameters for the glycine carboxyl group. The most distinctive feature of the studied systems is the presence of substantial net charge on the droplets. As Coulomb forces have a significantly higher range than the van der Waals forces, we increased the cutoff parameters for the interaction potential to an ultimate value comparable to the size of the entire droplet. Due to the largely increased number of interaction terms, this had a dramatic impact on computation time. In the CHARMM force field, as in most molecular modeling descriptions, the interaction potential utilizes an effective polarization for the particles. It has been shown that a more accurate treatment of the polarizabilities results in the enhancement of surface states at the liquid−vapor interface.[29,30]

Building Water Droplets. Despite its limited structural performance, we used the TIP3P water model because of the reduced computational cost.[31] Results of our validation simulations showed reasonable agreement with experimental quantities, and verified that this model was appropriate to study the behavior of charged nanodroplets. To build a water droplet, a coordinate file of a cube containing 125 water molecules was used. The coordinates of atoms in this water cube were obtained by Monte Carlo simulation and the equilibrium was completely reached for 300 K and periodic boundary conditions. Larger cubes were obtained by parallel translations of this cube along coordinate axes. After all the water molecules exceeding a particular distance measured from the center of the cube were removed, spherical droplets of different radii were obtained. Typically, droplets were composed of ~1000 to ~5000 water molecules.

Equilibration of the System. To generate the initial coordinates and velocities of ions within the droplet, we simulated the ion movement in a restraining spherical potential at high temperature with no solvent present. This ensured that ion distributions consistent with the dominant Coulomb interactions were rapidly attained. Then the ions were placed inside a preequilibrated water droplet and, in the case of overlap, water molecules were deleted from the system. Because the positions of the molecules in the combined system were artificial, the potential energy of the system was minimized and the new coordinates for all the atoms were calculated by annealing the system. For each droplet size, the total number of diglycine and/or hydronium ions was selected near the Rayleigh limit (for a Rayleigh limit calculator see http://home.gwu.edu/~mnelu/rayleigh.html). In most cases, this charge density led to at least one ion formation event during the first ~100 ps of simulation.

Model Verification. Figure 1 shows the calculated O−O radial distribution function, $g_{OO}(r)$, for a water droplet containing 4506 water molecules and compares it with neutron diffraction data.[32] The position of the first maximum of the calculated $g_{OO}(r)$ was in acceptable agreement with neutron diffraction data, although the calculations indicated slightly stronger correlation in this region. The second maximum observed in the experiments, however, was missing in the calculated data, showing that the model did not account for the second self-solvation shell in water.

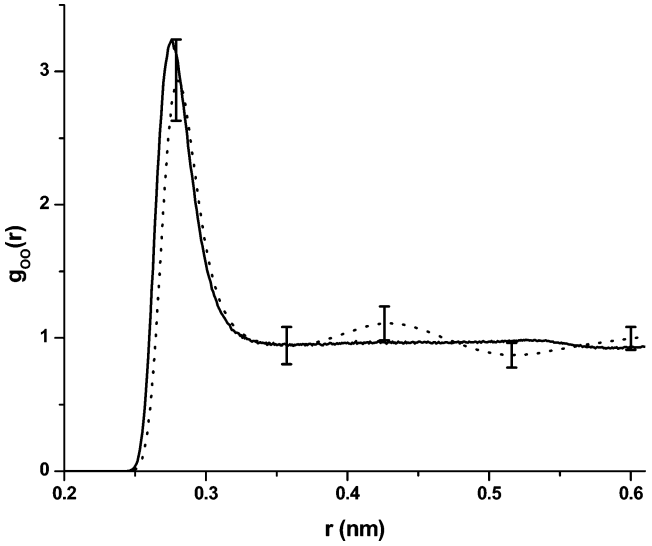

Figure 1. Calculated (solid line) radial distribution function, $g_{OO}(r)$, compared to experimental results and their uncertainty (dotted line, from ref 32).

The calculated enthalpy of evaporation for water at 300 K was 41.44 kJ/mol. This was ~6% lower than the 43.95 kJ/mol value observed in experiments. Similar relative errors had been observed for the enthalpy of sublimation of organic crystals.[25,26] The reduced evaporation enthalpy of water molecules resulted in a slightly increased rate of water evaporation in our calculations.

The experimental value of the self-diffusion coefficient of pure liquid water under ambient conditions is 2.30×10^{-5} cm^2 s^{-1}.[33] A value very close to the experimental one (2.62×10^{-5} cm^2 s^{-1}) may be obtained using the TIP5P model at 25 °C and 1 atm. However, for the water model used in CHARMM (TIP3P), a diffusion constant of 5×10^{-5} cm^2 s^{-1} had been reported under standard conditions.[34] We used the Einstein−Smoluchowski equation to calculate the self-diffusion coefficient of water molecules in a pure water droplet. The calculated 4.9×10^{-5} cm^2 s^{-1} self-diffusion coefficient was in good agreement with the literature value for TIP3P water. This value showed that during a 100 ps simulation a water molecule could traverse through the entire interior of the largest droplets we investigated.

Results

Droplet Structure. Rayleigh limit calculations predict that a water droplet composed of ~4500 molecules becomes unstable when the overall net charge equals 23 elementary charges. In real droplets, additional ions and their counterions might also be present, which would introduce a secondary effect on the droplet stability problem through the Debye screening of the excess charges.

Some of the most intriguing results were obtained when ion distributions inside the nanodroplets were analyzed. For example, structural differences were observed between a water droplet with ~6 nm initial diameter containing 23 hydronium ions and a similar droplet containing 2 hydronium ions and 21 diglycine ions. Figure 2 demonstrates several aspects of these differences. In both cases, an initial increase in droplet diameter was observed because of the general loosening of the droplet structure. According to conventional wisdom, the excess charges and their hydration shell are expected to be on the surface. Surprisingly, some of the ions were distributed inside the droplet and very few could be found within a solvation radius below the surface (Figure 2A). The hydronium ion layers were close

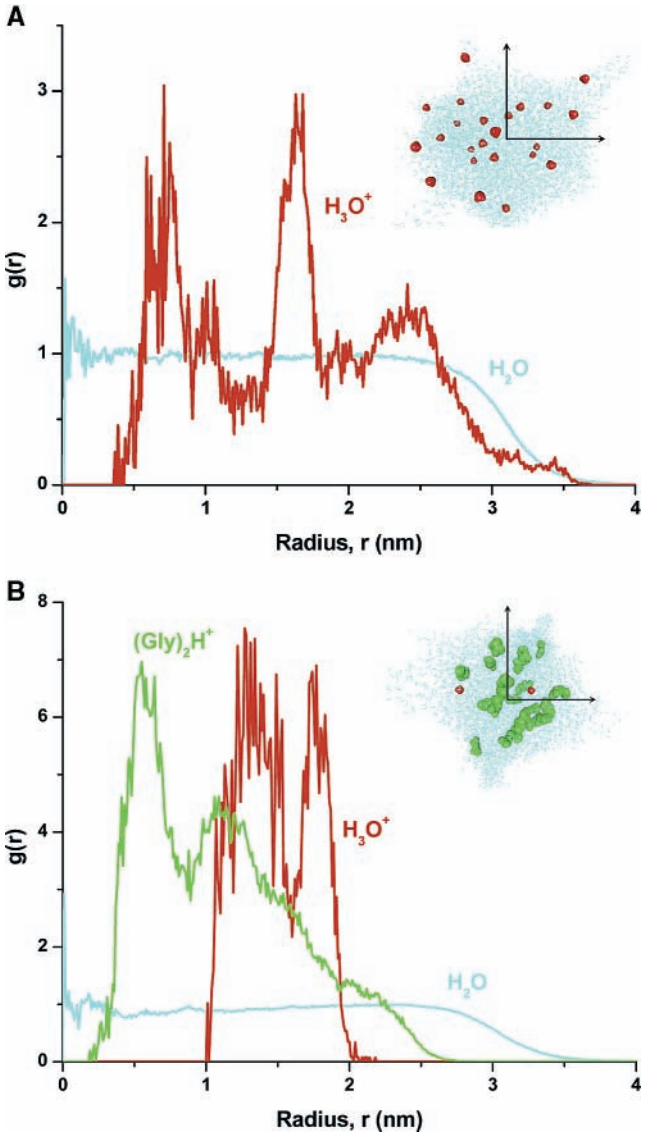

Figure 2. Radial distribution of water molecules and ionic species around the center of the nanodroplet reveal a well-defined structure (solid lines). A gradual drop in the radial distribution of the water molecules at the surface indicates that the outermost 0.5 nm layer is diffuse. Although the ions are spread inside the droplet, none is found in the center and only a few of them are close to the surface. (A) The droplet contains 23 hydronium ions that occupy three spherical layers (dotted line). (B) The droplet contains 21 diglycine ions that aggregate near the center of the droplet and 2 hydronium ions that stay closer to the surface. The insets show the actual arrangement of ions within the droplet.

to equally spaced, forming an onion shell-like structure, coherent with the expected tendency of ions to maximize their distance from each other. The calculated pH = 0.6 of these droplets may seem very low, but in analytical applications of ESI it is common practice to strongly acidify the initial solution using, e.g., trifluoroacetic acid. Furthermore, solvent evaporation from the original solution continuously lowers the pH.

When most of the hydronium ions were replaced by $(Gly)_2H^+$, fewer ions were found close to the surface of the droplet (Figure 2B). Although diglycine ions are more hydrophobic than hydronium ions, they concentrated more toward the center of the droplet. The hydronium ions preferred the spherical layer between 1 and 2 nm, whereas the diglycine ion distribution spanned from 0.5 to 2.5 nm. The probability of finding diglycine ions was highest inside the sphere of radius 2 nm, having two maxima for radii of 0.6 and 1.1 nm. In reality, the charge

distribution inside the droplet would also be influenced by external fields that are not considered here.

The latter simulation might raise important questions. First, is it possible that most of the net charge in the droplet consists of analyte ions? This question will be answered later in light of the relative evaporation rates of the analyte and hydronium ions. Second, how does the electrospray process produce nanodroplets with such a high analyte concentration? In electrospray, the initial analyte concentration is $\sim 10^{-5}$ M, whereas the concentration of analyte in the above-mentioned simulation is 0.27 M. It is clear from the dynamics simulation (see later) that the evaporation rate of the solvent is significantly higher than the evaporation rate of the analyte. Therefore, significant concentration of the analyte ions takes place during the evolution of the droplet. The actual degree of the concentration process, however, is not known.

The charge distribution was intriguing mainly because we expected to find the charge as close to the surface as possible. The presence of charges inside the droplet may be easily explained by considering a simple two-dimensional model in which charges with zero kinetic energy are placed within a circle in a vacuum. Two charges would obviously repel each other and try to stay at diametrically opposed positions. New charges added to the system would be equally spaced and form an equilateral triangle, a square, etc. These charges form a shell and the distance between them decreases as more charges are added. At some point, adding a charge on the surface would increase the potential of the system more than adding the same charge in the center. Figure 3A shows the potential difference, ΔE, between the two configurations for such systems as a function of the number of charges. The number of charges can be increased up to 11 with all of them staying on the surface. The 12th charge added to the system has a lower potential energy in the center than on the surface. Additional charges occupy positions within the circle by displacing the charge in the center and creating a shell-like structure.

In addition to the global minimum, this problem has some solutions representing local minima that may lead to metastable states. For example, in the case of 11 charges a metastable state can develop where not all the charges are on the circumference. Figure 3B presents the change in potential while moving one charge from the center (relative radius 0) to the circumference (relative radius 1). For each new position of the charge, the positions of all the other charges were recalculated to minimize the potential of the system. It is clear that the potential barrier ($\Delta E_{11}^{\#}$) is much higher than the difference in potential between the two extreme cases (ΔE_{11}). As a result, a charge might become trapped within the circle even though the potential of the system is slightly larger than for the case when all the charges are on the circumference. When additional charges are present, two or more charges may get confined by the potential barrier of the charges on the circumference. When water is introduced instead of the vacuum environment, the interaction between the charges is reduced and more charges may be placed on the circumference. However, further increasing the number of charges results in energetically favored positions inside the circle.

For both the global minimum and for the metastable cases, the charges inside the circle will assume symmetric configurations around the center. For example, three charges would form a triangle, which could be seen as a new layer of charges inside the outer layer. All the above considerations may be generalized to the three-dimensional idealized case of no thermal motion. Clearly, a significant degree of Debye-screening, large droplet

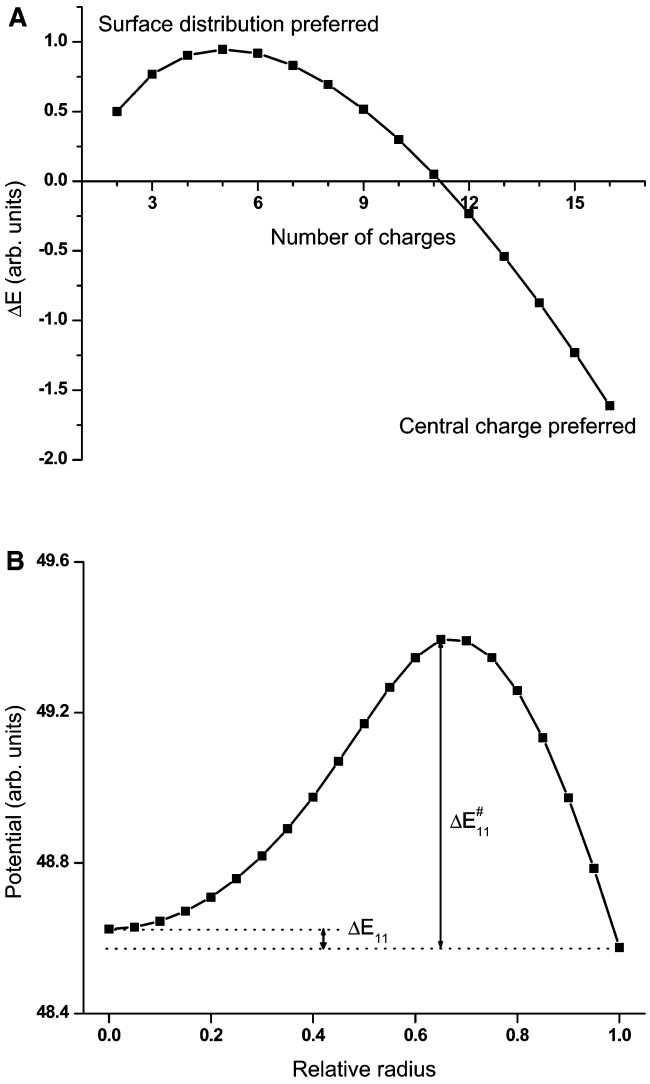

Figure 3. Potential energy difference, ΔE, between the configuration with all the charges on the surface and the configuration where one of the charges is moved to the center. Adding a charge on circumference of a circle is favored over adding the charge in center of the circle up to 11 total charges. For more than 11 charges, the configuration with one charge in center has a lower potential (A). When a charge is moved from center to the circumference, the potential barrier, $\Delta E^{\#}_{11}$, is much larger than the difference in potential of the two extremes, ΔE_{11} (B).

size, and/or increased temperature can blur the shell structure into a more conventional monotonic distribution. We can use a similar argument to explain the shell-like structure of charges we observe in the simulations.

The orientation of the diglycine ions could be affected by two factors. For a minimum potential energy, the charges on the amino-termini should stay as far from one another as possible and, conventionally, they should be on or close to the surface of the droplet. The middle part of the ion is less hydrophilic than the amino and the carboxyl termini, so it should also be close to the surface. Radial distribution functions calculated for the two ends of the diglycine ions did not show a preferred orientation of these ions inside the droplet.

Dynamics of Charge Reduction. Visualization of the simulations showed that at the molecular scale, the surface of a charged nanodroplet was neither spherical nor smooth. Instead, it exhibited large-scale deformations as well as protrusions and depressions fluctuating in time. Figure 4A presents in spherical coordinates the surface map of a 6 nm pure water droplet after a 30 ps simulation of its evolution. A map for a second droplet,

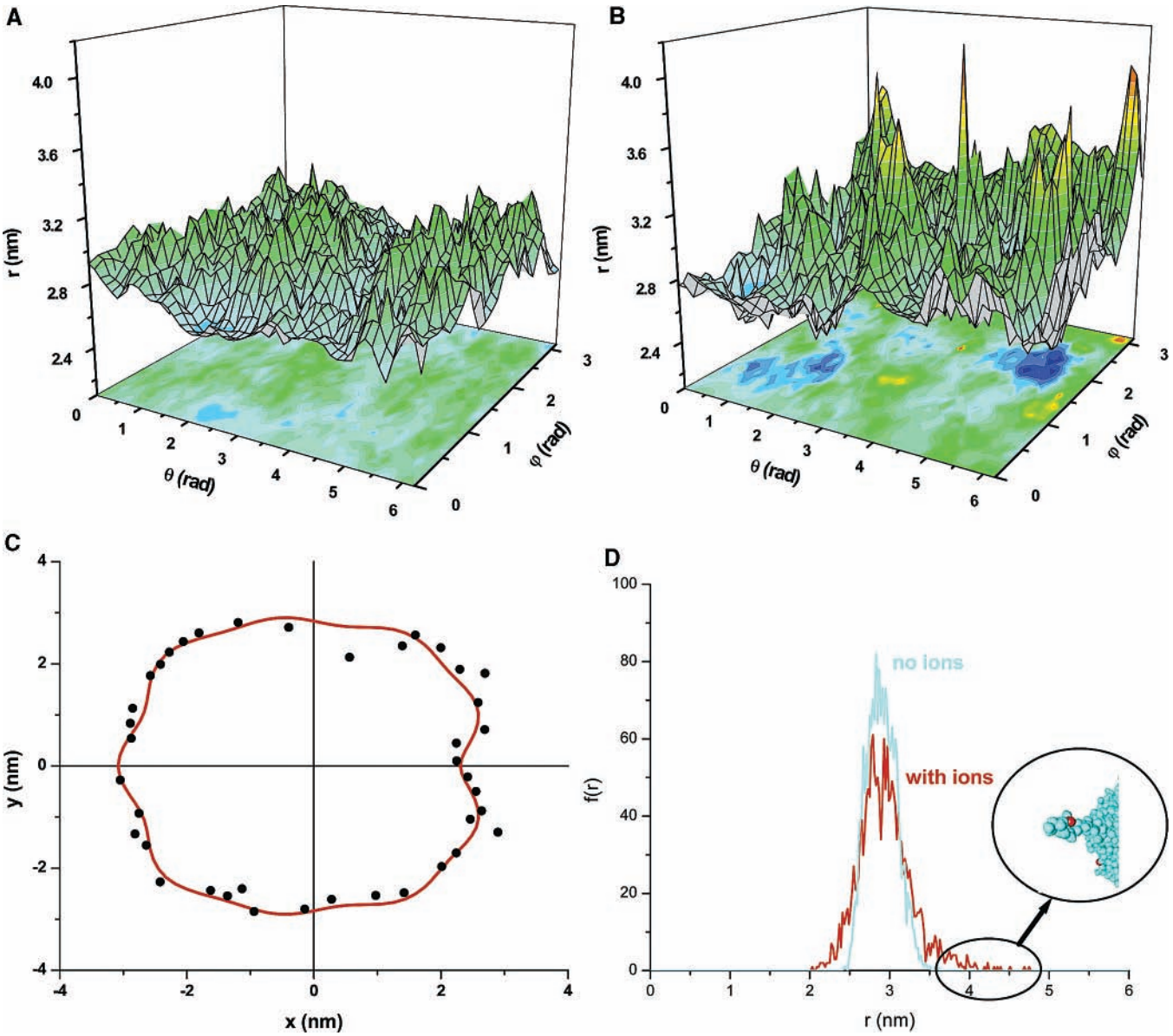

Figure 4. Snapshots of the surface of 6 nm droplets in spherical coordinates showing the formation of deformations as well as protrusions and depressions. The presence of ions inside the nanodroplet induces surface fluctuations of higher amplitude (B) than the thermal fluctuations produced in a pure water droplet (A). Panel C is an equatorial sectional view of a charged droplet indicating the overall deformations and the local protrusions. Linear combination of Legendre polynomials, $\sum_l a_l P_l(\cos\theta)$, are used to fit the contour ($a_1 = 2.92$ nm, $a_2 = -0.147$ nm, $a_5 = -0.228$ nm, $a_{10} = -0.239$ nm). The spherical core of the droplet is represented by the first term, a_1P_1. Lower order terms, a_2P_2 and a_5P_5 describe the deformations, whereas the protrusions are reflected in the high order term, $a_{10}P_{10}$. Panel D depicts the distribution of radial distance of water molecules on the surface from the center of droplet. The tailing in both directions in the presence of ions indicates their role in destabilizing the droplet morphology. Extreme amplitude protrusions (see inset) may result in the detachment of solvated ions.

similar in size, but containing 23 hydronium ions is shown in Figure 4B. Clearly, significantly higher amplitude fluctuations developed when ions were present in the droplet. The visualization of a 3 ps evolution of the charged droplet surface is available as Supporting Information.

Figure 4C shows an equatorial sectional view of the charged nanodroplet with only the surface molecules represented. In this plane, the radial position of surface molecules due to capillary waves, r, can be expanded in spherical harmonics:

$$r = \sum_l r^0{}_l \, Y_l(\theta,\varphi{=}0) \cos(\omega_l t + \epsilon_l)$$

where $r^0{}_l$ is the amplitude of the lth component and ω_l and ϵ_l are the circular frequency and the phase of the lth wave, respectively. The lth normalized spherical harmonic is expressed by Legendre polynomials:

$$Y_l(\theta,\varphi{=}0) = \sqrt{\frac{2l+1}{4\pi}} P_l(\cos\theta)$$

In Figure 4C, for a particular time frame a linear combination of Legendre polynomials, $\sum_l a_l P_l(\cos\theta)$, are used to describe the droplet morphology. The most significant of the first 10 a_l amplitudes, $a_1 = 2.92$ nm, $a_2 = -0.147$ nm, $a_5 = -0.228$ nm, and $a_{10} = -0.239$ nm, are determined using multiple regression. The first term, a_1P_1, describes the remaining spherical character of the droplet. As is clear from the presence of the other low order terms a_2P_2 and a_5P_5 in the Legendre expansion, considerable departure from the spherical shape is observed. These large-scale deformations can become dominant for significantly supercharged droplets and lead to partitioning of the charge on comparable sized fission products. However, large amplitude fluctuations of small area protrusions, described, for example,

by the higher order term $a_{10}P_{10}$ in the Legendre expansion, are instrumental in charge reduction at the Rayleigh limit. These protrusions, as shown later, are instrumental in charge reduction through the ejection of solvated ions.

To assess the statistical weight of these extreme protrusions, Figure 4D compares the radial positions of molecules on the surface of the two droplets. The distance of surface molecules from the center extended over a larger interval of radii in the case of the droplet containing ions than in the case of pure water. For the water droplet, the amplitude of thermal fluctuations can be expressed as

$$2\Delta r = 2\sqrt{\frac{kT}{\gamma}} = 0.48 \text{ nm}$$

where the surface tension of water at 300 K is $\gamma = 0.07$ N/m. The fwhm of a Gaussian fit to the blue curve in Figure 4D provides 0.41 nm, a remarkable agreement. Thus, the surface irregularities on a pure water droplet can be fully ascribed to thermal fluctuations. Therefore, the formation of deeper holes and especially larger amplitude protrusions on the droplet surface (red curve in Figure 4D) can be attributed to the presence of ions.

On the basis of the theoretical description of capillary waves on the surface of charged droplets, irregular droplet shapes and shape fluctuations are expected.[23] A nonlinear analysis of surface fluctuations reveals that the characteristic time of the spheroidal buildup for a droplet is

$$\tau_0 = R^2\sqrt{\frac{\rho}{2\Delta r\gamma}} + \frac{\nu\rho}{34\gamma}\sqrt{\frac{R^5}{\Delta r^3}}$$

where at $T = 300$ K for liquid water the density, $\rho = 996$ kg/m^3, and $\nu = 0.85 \times 10^{-6}$ m^2/s is the kinematic viscosity.[35] For an $R \approx 3$ nm water droplet at the Rayleigh limit, τ_0 is predicted to be ~100 ps, a value that is within the scope of our calculations. A slight spheroidal buildup is clearly observed in the case of the charged droplets, as evidenced by the amplitude of low order Legendre polynomials that describe their shape.

To follow the prevailing charge reduction mechanism in ESI, we simulated the dynamics of nanodroplets containing different number of ions. If we used a number of ions much lower than the Rayleigh limit, no ion evaporation from the nanodroplet was observed during the simulation time. Generally, ion evaporation was observed for a charge density slightly lower than or equal to the Rayleigh limit, although in some simulations no ion evaporation took place during the simulation time even for charge densities equal to the Rayleigh limit. Coulomb explosion took place if the charge density of the droplet was significantly higher than the Rayleigh limit: a violent breakup of the droplet was observed for nanodroplets containing a high number of singly charged ions or a smaller number of multiply charged ions. These results (to be presented in a separate publication) indicated that the charge residue model was feasible for supercharged droplets, whereas the solvated ion evaporation model was more adequate for droplets close to the Rayleigh limit.

For example, in the case of critically charged droplets at 300 K thermally induced protrusions were observed on the surface. In turn, these protrusions facilitated the departure of ions. First, the ions induced the enlargement of these protrusions on the droplet surface (Figure 5A). Next, some ions were pushed by electrostatic repulsion from the droplet along or into the protrusion toward lower potential points leading to ion separation (Figure 5B). Finally, when the repulsion between the rest of the droplet and the separated ion exceeded the cohesive forces within the protrusion, the solvated ion detached (Figure 5C). To visualize this mechanism, parts D−F of Figure 5 show the distribution of the ions inside the droplet. A similar animation showing the evaporation of a diglycine ion is available as Supporting Information. Extreme protrusions play a similar role in this mechanism to "fingers" found at liquid interfaces. Modeling studies indicate that ion transport from water to the organic phase proceeds through water "fingers" that extend into the organic phase.[36]

During a ~130 ps simulation of a 6 nm droplet containing 23 hydronium ions, three hydronium ions evaporated. During a similar period, the same number of hydronium ions evaporated from a similar nanodroplet containing 21 hydronium ions and 2 diglycine ions, but no ion evaporated from a nanodroplet containing 2 hydronium ions and 21 diglycine ions.

These observations suggest that a significant factor in the evaporation process is the mobility and/or size of the ions in the system. In fact, the mobility of the hydronium ion is even higher than represented in the calculations due to proton tunneling. As a result, the departure of hydronium ions is expected to be more frequent than predicted by our calculations.

The present model did not account for the change in peptide protonation equilibrium due to pH change.[37] Two processes influence the pH of the droplets in opposite direction. The pH of the droplet increases as the hydronium ions evaporate, inducing an equilibrium shift toward the deprotonation of the peptide. At the same time, solvent evaporation decreases the pH of the droplet, which facilitates the opposite process. Competition between these processes is likely to have a profound effect on ion formation in electrospray.

Because no diglycine ion evaporation occurred during the simulation time from a relatively large droplet even for large analyte concentrations, we expected that the peptide ion would evaporate only after the droplet became smaller due to its evaporative shrinking. The MD simulation of a ~4 nm diameter droplet (Rayleigh limit = 13 charges) containing 11 hydronium ions and 2 diglycine ions indicated the evaporation of 4 hydronium ions during the first 300 ps. From a similar droplet containing 2 hydronium ions and 11 diglycine ions, a diglycine ion and both hydronium ions evaporated within ~160 ps.

The data presented here support the solvated ion evaporation model for the studied systems. For mixtures, the mobility/size of the ion seems to be more important in determining the ion evaporation rate than its hydrophobicity. Even at ~10 times lower concentrations, the hydronium ion evaporates faster from small-size droplets than the diglycine ion. Of course, for ions with comparable mobilities, hydrophobicity remains an important factor.

Several promising follow-up studies are envisioned; some of them are already underway. The presented simulations can be readily extended to the investigation of charged nanojets. Elongated droplets have been observed as the product of Coulomb fission. These objects can be viewed as stretched out spheroids prone to further division. The analysis of nanojet deformations would be instructive regarding the presence of correlations between the different generations in a division cascade. Furthermore, the interaction of individual droplets, a potentially important process in dense ESI plumes, can also be studied. Polarization of droplets by each other can lead to deformations and induce fission below the Rayleigh limit. The introduction of counterions and/or macromolecular ions of different hydrophobicity is another promising line of inquiry

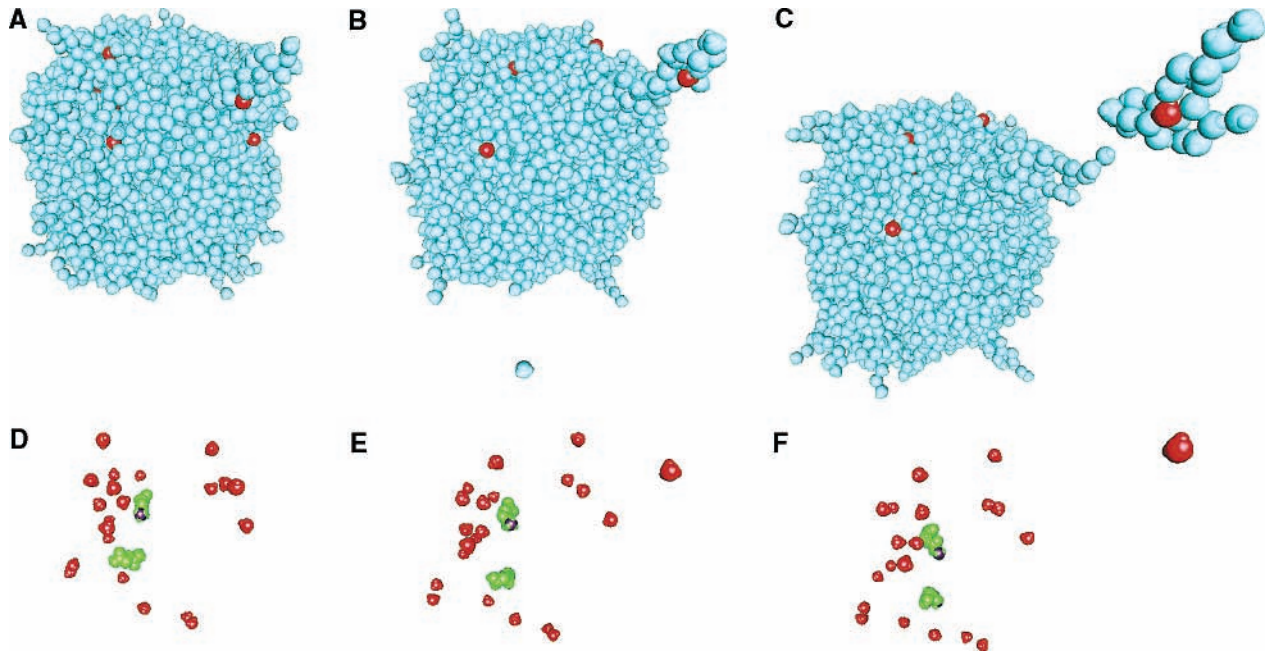

Figure 5. Detachment of a water cluster containing a single hydronium ion from a critically charged nanodroplet composed of 4300 water molecules (blue), 21 hydronium ions (red) and 2 diglycine ions (green). Snapshots were taken before (33 ps, A and D), at the formation (43 ps, B and E), and after the detachment (46 ps, C and F) of an extreme amplitude protrusion containing an ion. Ion distributions inside droplet are shown in panels D−F.

as the segregation of various ions in a charged droplet has important implications for ion generation in mass spectrometry as well as for atmospheric processes.

Acknowledgment. Helpful discussions with Drs. Akos Bencsura and Karoly Vekey (Chemical Research Center of the Hungarian Academy of Sciences, Hungary) regarding the use of the CHARMM code and the two-dimensional demonstration of charge distributions in confined space, respectively, are acknowledged. Dr. John Callahan of the Naval Research Laboratory is thanked for his insightful comments on the manuscript. Partial funding for this work was provided by grants from the National Science Foundation (CHE-9873610), from the Department of Energy (DE-FG02-01ER15129), and by the Research Enhancement Fund of the George Washington University.

Supporting Information Available: Two movies showing a 3 ps segment from the surface evolution of a charged nanodroplet (Vertesmov1.mov) and the solvated ion evaporation process (Vertesmov2.mov). This material is available free of charge via the Internet at http://pubs.acs.org.

References and Notes

(1) Geldart, D. J. W.; Chýleka, P. *J. Quant. Spectr. Radiat. Transf.* **2001**, *70*, 697−708.
(2) Navarro-González, R.; Ramfrez, S. I. *Adv. Space Res.* **1997**, *19*, 1121−1133.
(3) Tripathi, S. N.; Harrison, R. G. *Atmosph. Environ.* **2001**, *35*, 5817−5821.
(4) Rayleigh, L. *Proc. R. Soc. London* **1878**, *28*, 405−409.
(5) Rayleigh, L. *Proc. R. Soc. London* **1879**, *29*, 71−97.
(6) Rayleigh, L. *Philos. Mag.* **1882**, *14*, 184−186.
(7) Taylor, G. *Proc. R. Soc. London A* **1964**, *280*, 383−397.
(8) Yamashita, M.; Fenn, J. B. *J. Phys. Chem.* **1984**, *88*, 4451−4459.
(9) Fenn, J. B.; Mann, M.; Meng, C. K.; Wong, S. F.; Whitehouse, C. M. *Science* **1989**, *246*, 64−71.
(10) Valaskovic, G. A.; Kelleher, N. L.; Little, D. P.; Aaserud, D. J.; McLafferty, F. W. *Anal. Chem.* **1995**, *67*, 3802−3805.
(11) Jarrold, M. F. *Annu. Rev. Phys. Chem.* **2000**, *51*, 179−207.
(12) Wyttenbach, T.; Witt, M.; Bowers, M. T. *J. Am. Chem. Soc.* **2000**, *122*, 3458−3464.
(13) Counterman, A. E.; Clemmer, D. E. *J. Phys. Chem. B* **2001**, *105*, 8092−8096.
(14) Cole, R. B. *J. Mass. Spectrom.* **2000**, *35*, 763−772.
(15) Kebarle, P. *J. Mass. Spectrom.* **2000**, *35*, 804−817.
(16) Juraschek, R.; Röllgen, F. W. *Int. J. Mass Spectrom. Ion Processes* **1998**, *177*, 1−15.
(17) Gomez, A.; Tang, K. *Phys. Fluids* **1994**, *6*, 404−414.
(18) Dole, M.; Mack, L. L.; Hines, R. L. *J. Chem. Phys.* **1968**, *49*, 2240−2249.
(19) Iribarne, J. V.; Thomson, B. A. *J. Chem. Phys.* **1976**, *64*, 2287−2294.
(20) Gamero-Castano, M.; Fernandez de la Mora, J. *J. Mass Spectrom.* **2000**, *35*, 790−803.
(21) Gamero-Castano, M.; Fernandez de la Mora, J. *J. Chem. Phys.* **2000**, *113*, 815−832.
(22) Fernandez de la Mora, J. *Anal. Chim. Acta* **2000**, *406*, 93−104.
(23) Shiryaeva, S. O.; Grigor'ev, A. I.; Belonozhko, D. F. *Tech. Phys. Lett.* **2000**, *26*, 857−860.
(24) Chech, N. B.; Enke, C. G. *Anal. Chem.* **2000**, *72*, 2717−2723.
(25) Sadeghi, M.; Wu, X.; Vertes, A. *J. Phys. Chem. B* **2001**, *105*, 2578−2587.
(26) Wu, X.; Sadeghi, M.; Vertes, A. *J. Phys. Chem. B* **1998**, *102*, 4770−4778.
(27) MacKerell, A. D., Jr.; Bashford, D.; Bellott, M.; Dunbrack, R. L., Jr.; Evanseck, J. D.; Field, M. J.; Fischer, S.; Gao, J.; Guo, H.; Ha, S.; Joseph-McCarthy, D.; Kuchnir, L.; Kuczera, K.; Lau, F. T. K.; Mattos, C.; Michnick, S.; Ngo, T.; Nguyen, D. T.; Prodhom, B.; Reiher, W. E., III.; Roux, B.; Schlenkrich, M.; Smith, J. C.; Stote, R.; Straub, J.; Watanabe, M.; Wiórkiewicz-Kuczera, J.; Yin, D.; Karplus, M. *J. Phys. Chem. B* **1998**, *102*, 3586−3616.
(28) Bilalbegovic, G.; Lutz, H. O. *Chem. Phys. Lett.* **1997**, *280*, 59−65.
(29) Dang, L. X.; Chang, T.-M. *J. Phys. Chem. B* **2002**, *106*, 235−238.
(30) Jungwirth, P.; Tobias, T. J. *J. Phys. Chem. A* **2002**, *106*, 379−383.
(31) Jorgensen, W. L.; Chandrasekhar, J.; Madura, D. J.; Impey, R. W.; Klein, M. L. *J. Chem. Phys.* **1983**, *79*, 926−935.
(32) Soper, A. K. *Chem. Phys.* **2000**, *258*, 121−137.
(33) Mills, R. *J. Phys. Chem.* **1973**, *77*, 685−688.
(34) Sorenson, J. M.; Hura, G.; Glaeser, R. M.; Head-Gordon, T. *J. Chem. Phys.* **2000**, *113*, 9149−9161.
(35) Shiryaeva, S. O. *Tech. Phys.* **2000**, *45*, 1128−1134.
(36) Benjamin I. *Annu. Rev. Phys. Chem.* **1997**, *48*, 407−451.
(37) Zhou, S.; Edwards, A. G.; Cook, K. D.; Van Berkel, G. J. *Anal. Chem.* **1999**, *71*, 769−776.